




MR imaging profile and histopathological characteristics of tumour vasculature, cell density and proliferation rate define two distinct growth patterns of human brain metastases from lung cancer

Makoto Kiyose^{1,2,3,4} · Eva Herrmann⁵ · Jenny Roesler⁶ · Pia S. Zeiner^{2,3,4,7,8,9} · Joachim P. Steinbach^{3,4,7,8,9} · Marie-Therese Forster¹⁰ · Karl H. Plate^{6,8,9} · Marcus Czabanka¹⁰ · Thomas J. Vogl¹¹ · Elke Hattingen¹ · Michel Mittelbronn^{6,12,13,14,15,16,17} · Stella Breuer¹ · Patrick N. Harter^{6,8,9} · Simon Bernatz^{3,4,6,11} 

Received: 23 July 2022 / Accepted: 26 September 2022 / Published online: 3 October 2022
© The Author(s) 2022

Abstract

Purpose Non-invasive prediction of the tumour of origin giving rise to brain metastases (BMs) using MRI measurements obtained in radiological routine and elucidating the biological basis by matched histopathological analysis.

Methods Preoperative MRI and histological parameters of 95 BM patients (female, 50; mean age 59.6 ± 11.5 years) suffering from different primary tumours were retrospectively analysed. MR features were assessed by region of interest (ROI) measurements of signal intensities on unenhanced T1-, T2-, diffusion-weighted imaging and apparent diffusion coefficient (ADC) normalised to an internal reference ROI. Furthermore, we assessed BM size and oedema as well as cell density, proliferation rate, microvessel density and vessel area as histopathological parameters.

Results Applying recursive partitioning conditional inference trees, only histopathological parameters could stratify the primary tumour entities. We identified two distinct BM growth patterns depending on their proliferative status: Ki67_{high} BMs were larger ($p = 0.02$), showed less peritumoural oedema ($p = 0.02$) and showed a trend towards higher cell density ($p = 0.05$). Furthermore, Ki67_{high} BMs were associated with higher DWI signals ($p = 0.03$) and reduced ADC values ($p = 0.004$). Vessel density was strongly reduced in Ki67_{high} BM ($p < 0.001$). These features differentiated between lung cancer BM entities ($p \leq 0.03$ for all features) with SCLCs representing predominantly the Ki67_{high} group, while NSCLCs rather matching with Ki67_{low} features.

Conclusion Interpretable and easy to obtain MRI features may not be sufficient to predict directly the primary tumour entity of BM but seem to have the potential to aid differentiating high- and low-proliferative BMs, such as SCLC and NSCLC.

Keywords Brain metastasis · Magnetic resonance imaging · Imaging biomarker · Tumour vasculature · Histopathology

Introduction

Brain metastases (BMs) are the most common intracranial neoplasms in adults showing an increasing incidence [1–3]. BMs are usually associated with an advanced tumour stage as well as high patient morbidity and mortality. Despite complex multimodal treatment approaches including surgery, stereotactic radiosurgery or whole brain irradiation, overall survival of patients with BM still remains poor, often not exceeding 6 months [4], and only a small proportion of

patients show long-term survival [4]. In patients presenting with a cancer of unknown primary and a single intracranial metastasis, magnetic resonance imaging (MRI) diagnosis of BM is particularly challenging. In case of single metastases, it might be difficult to differentiate them from malignant primary brain tumours or brain abscess [5, 6]. Some studies described hypointense T2-weighted imaging signal in adenocarcinomas and investigated related histopathological features [7, 8]. Previous histopathological and MR neuroimaging studies investigated the prognostic value of single parameters such as brain oedema [9, 10].

Signal intensities or lesion pattern on conventional MRI or other MRI parameters such as water diffusion may aid in the characterisation of diseased brain tissue. Reduced apparent diffusion coefficient (ADC) in brain tumours,

✉ Simon Bernatz
Simon.Bernatz@kgu.de

Extended author information available on the last page of the article

calculated from diffusion-weighted imaging (DWI) [11], is found in areas with higher cell density, since the increased number of cells narrow the extracellular space [12–14]. Consequently, DWI parameters correlate with histopathological characteristics of primary brain tumours, such as tumour entity, tumour grading [15] and Ki67 tumour cell proliferation index [16]. However, it is unclear if DWI and other MRI patterns may have the potential to allow for the differentiation of the BM primary tumour entity. Such a differentiation would ease the diagnostic workup. For example, inconclusive biopsies of lung cancers may implicate surgery of BM that however would not be the first choice in small-cell lung cancer (SCLC), since BMs of SCLC are predominantly treated by radiotherapy. In contrast, surgical resection of the primary lung cancer and solitary BM of non-small-cell lung cancer (NSCLC) is warranted (for review, see Goldberg et al. [17]).

In this study, we aimed to elucidate discriminators for BMs originating from different primary tumours by analysing their morphological MRI features, ADC values and signal intensities on DWI, T2-weighted and T1-weighted MR images. We correlated these MRI features with histopathological parameters to validate tumour biology and to elucidate the underlying mechanism.

Materials and methods

Patient cohort and clinical data

We retrospectively analysed 95 preoperative MRIs with histologically proven BM (female, 50; male, 45; mean age 59.6 ± 11.5 years) from malignant melanoma ($n=10$), breast cancer ($n=18$), NSCLC ($n=30$), SCLC ($n=8$), renal cell carcinoma ($n=7$), colon cancer ($n=7$), carcinomas not otherwise specified (NOS) ($n=10$) or others ($n=5$, including rare entities like ovary carcinoma and oesophageal carcinoma). All patients underwent surgical BM resection. Pre-operative Karnofsky Performance Scale (KPS) was assessed [18]. Median KPS was 80%, ranging from 20 to 100%.

MR imaging

MRI was performed in clinical routine at different institutions (in-house $n=53$; other institutions $n=42$) with different field strengths (1 Tesla $n=4$; 1.5 Tesla $n=57$; 3 Tesla $n=34$) and manufacturers (Siemens Healthineers $n=43$, Philips Healthcare $n=42$, General Electric Healthcare $n=10$), different slice thicknesses and gaps. The in-house and external MRI protocols included at least T1-weighted images with and without contrast enhancement and T2-weighted images. Further, DWI sequences were available in 79 MRIs with ADC parameter maps in 64 cases.

T2*-weighted and fluid attenuated inversion recovery sequences in 61 and 86 cases. Protocols, as well as contrast agent application, varied due to interinstitutional standardised operating procedures. We aimed to develop an approach that is feasible in clinical routine facing highly heterogeneous data.

MRI analysis

Assessment of peritumoural oedema

Peritumoural oedema was defined as a region of clear T2 signal hyperintensity adjacent to the tumour margin. Measurements were performed at the maximum extent of the oedema evaluable on the T2-weighted images in axial orientation according to former studies of Spanberger et al. [9] and Tung et al. [19] (Fig. 1).

Region of interest (ROI) placements

For quantitative measurements, we manually drew uniform ROIs in the largest visually delineable iso- or hypointense solid tumour part of the BM by reviewing the T2- and unenhanced T1-weighted images and their corresponding structures on the DWI and ADC parameter maps yielding normalised mean values.

Furthermore, we calculated the contrast-to-noise ratios ($T2_{CNR}$, $T1_{CNR}$, DWI_{CNR}) in reference to Hayashida et al. [20] by the formula: $\frac{(T2_{SI}^{mean} - T2^{WM})}{T2^{noise}}$ (only exemplarily shown for $T2_{CNR}$). ROI placements and calculations are displayed schematically in Fig. 2.

Size and contrast enhancement of the BM

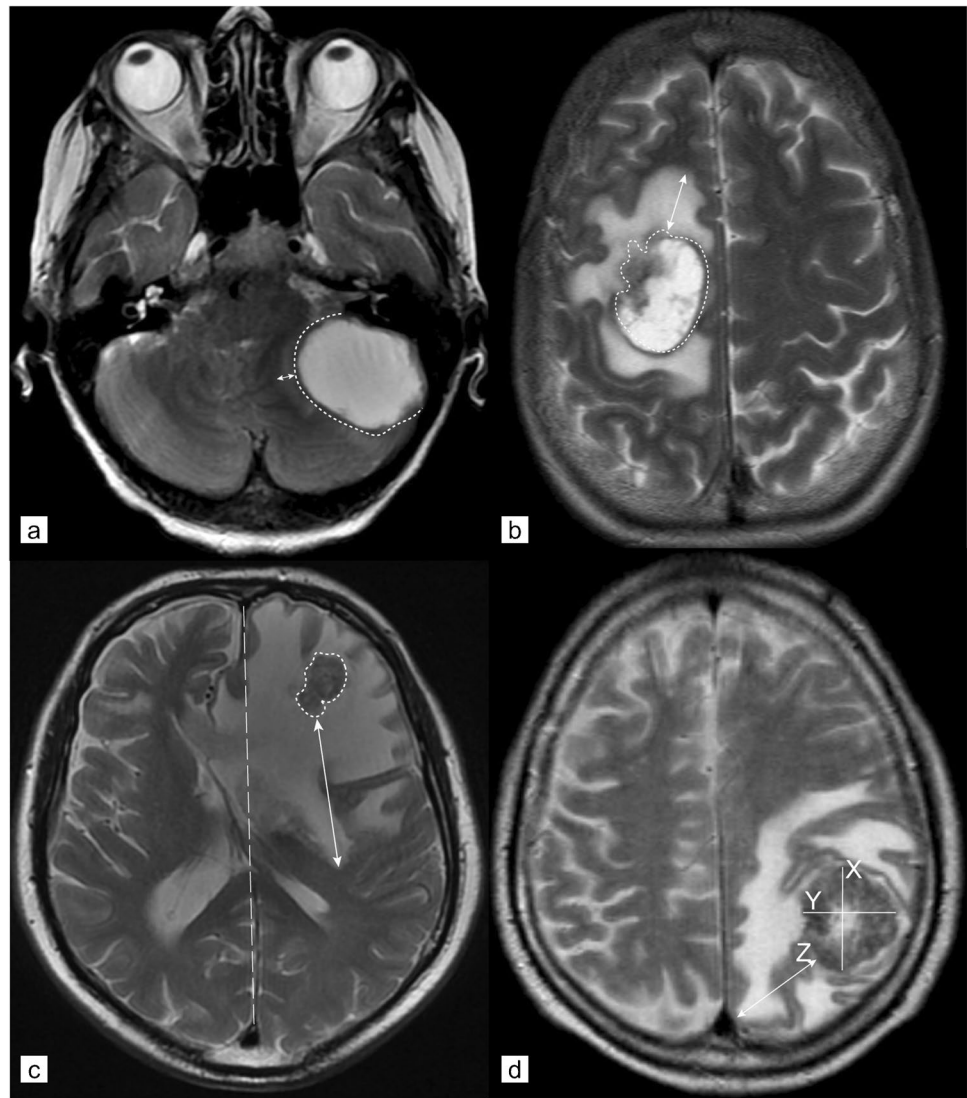
For assessment of BM size, we chose a slide showing the maximal extent of the lesion and measured the maximal unidimensional diameter (mm) on the axial contrast-enhanced T1-weighted images.

Histopathological analyses

Tissue specimens, processing and patient data

Neuropathological examination was performed by board certified neuropathologists (KHP, MM, PNH). We investigated formalin-fixed and paraffin-embedded BM tissue obtained from the University Centre of Tumour disease Biobank Goethe University, Frankfurt am Main, Germany, member of the German Cancer consortium. All stainings were performed on tissue micro arrays. The study protocol including the usage of biomaterial was endorsed by the local ethical committee (GS 4/09; SNO-04-2015).

Fig. 1 Oedema scoring. Overview of oedema scoring according to Spanberger et al. [9] and Tung et al. [19]. **a** T2-weighted MRI of a left-sided infratentorial brain metastasis with a very small peritumoural oedema (arrowed line) according to Spanberger grade 1 (maximal width 1 cm). **b** T2-weighted MRI of a right frontal metastasis with a moderate peritumoural oedema rim (arrowed line) according to Spanberger grade 2 (maximal width > 1 cm, but not crossing the midline of the brain). **c** T2-weighted MRI of a left frontal metastasis with a large peritumoural oedema (arrowed line) according to Spanberger grade 3 (maximal width > 1 cm rim and crossing the midline of the brain). **d** T2-weighted MRI with a left parietal metastasis. Example of measurements: (X) maximal orthogonal diameter, (Y) maximal horizontal diameter, (Z) maximal peritumoural oedema expansion measured from the margin of the metastasis. Peritumoural oedema ratio according to Tung et al. [19] is calculated as follows: ‘peritumoural oedema’ / (‘orthogonal diameter’ + ‘horizontal diameter’) / 2



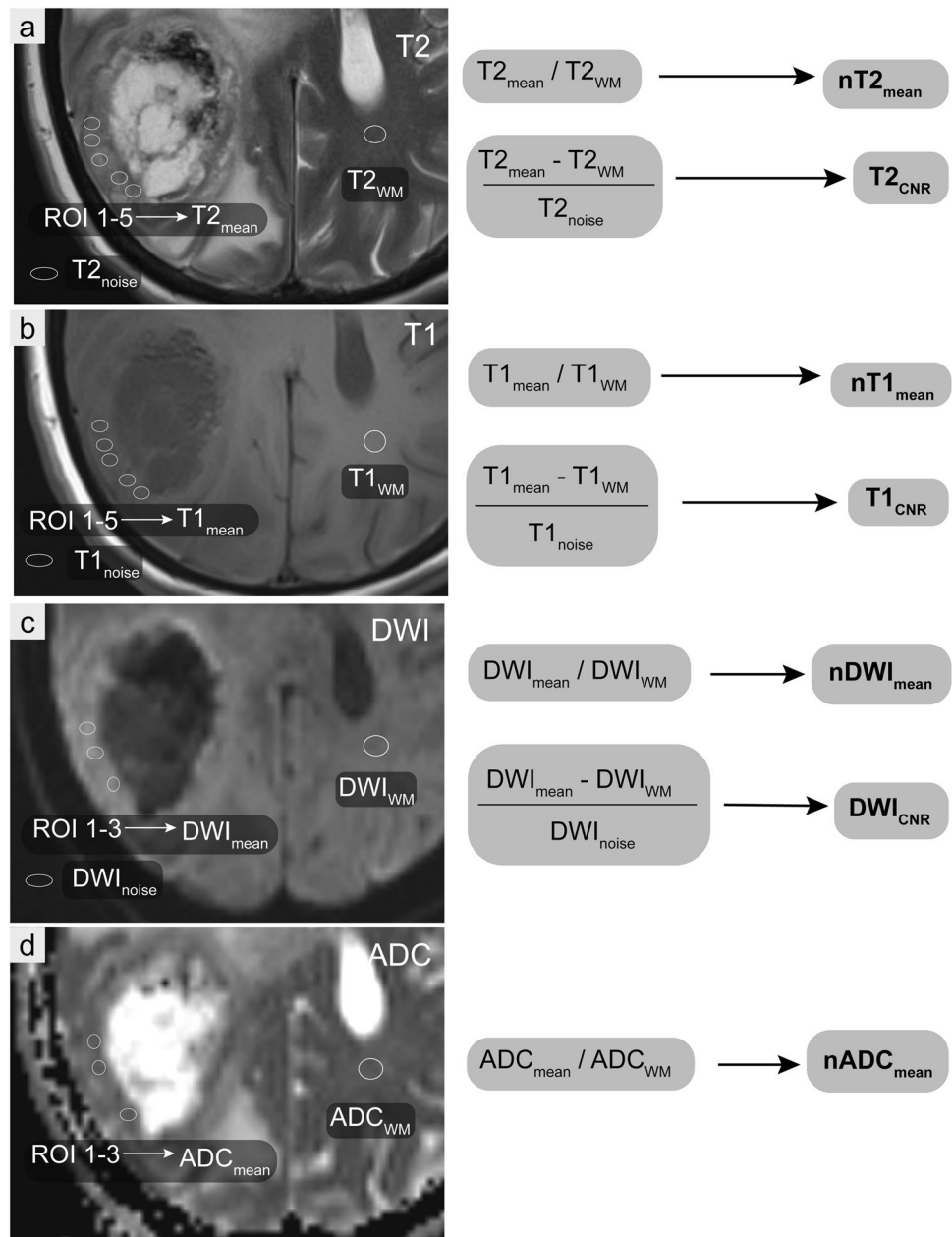
Immunohistochemistry and immunofluorescence

The tissue micro arrays were cut into 3 µm thick slices using a microtome (Leica Microsystems, Nussloch GmbH, Nussloch, Germany), placed on microscope slides (SuperFrost, Thermo Scientific, Dreieich, Germany), heated to 40 °C for 20 min (HI 1220, Leica Biosystems Nussloch GmbH, Nussloch, Germany) and stored at 37 °C overnight in an incubator (Heraeus, function line, B12, Thermo Electron Corporation, Waltham, Massachusetts, USA). Immunohistochemistry was executed using standardised protocols for the automated slide staining system Discovery XT (Roche/Ventana, Tucson, Arizona, USA) including antibodies against the following antigens: Ki67 (Dako) and CD31 (Dako). Slides were counterstained with haematoxylin and mounted. For cell density analyses, we performed a nuclear 4',6-diamidino-2-phenylindole (DAPI) staining following deparaffinisation.

Data analysis

Cell proliferation was assessed by Ki67 staining and analysed using an Olympus BX-50 (Hamburg, Germany) microscope. Raw data of Ki67 proliferation rate have already been published [21] and are now included for further analyses in comparison with neuroradiological parameters. Vessel density was analysed by counting cluster of differentiation (CD) 31-positive vascular structures in relation to the analysed tumour area (per mm²) using a light microscope with a Stereo Investigator (Version 4.34 software from MicroBrightField Inc.). Vessel area was analysed measuring CD31-positive vessel lumina. Data analyses were performed using ImageJ 1.48v (National Institute of Mental Health, Bethesda, Maryland, USA). For cell density measurement, representative images of tumour-bearing areas of the DAPI-stained tissue micro arrays were taken using a Nikon 80i microscope (Nikon, Düsseldorf, Germany) in a 200-fold magnification

Fig. 2 Workflow of region of interest definition and score calculation. Exemplary scheme of region of interest (ROI) placements and calculations on a right parieto-occipital brain metastasis. **a–b** Signal intensities of the solid tumour in the T2- (**a**) and T1- (**b**) weighted sequences were assessed by five ROIs. **c–d** The limited spatial resolution of the DWI (**c**) and ADC (**d**) parameter maps available allowed the assessment by no more than three ROIs. We documented the average of these ROIs ($T2_{\text{mean}}$, $T1_{\text{mean}}$, DWI_{mean} , ADC_{mean}). **a–d** Same-sized uniform ROIs were also drawn in the corresponding normal-appearing white matter of the contralateral hemisphere as reference values ($T2_{\text{WM}}$, $T1_{\text{WM}}$, DWI_{WM} , ADC_{WM}). Normalised values were established as ratios to the reference ROI yielding ($nT2_{\text{mean}}$, $nT1_{\text{mean}}$, $nDWI_{\text{mean}}$, $nADC_{\text{mean}}$). Further, we drew one ROI in the surrounding air outside the head taking its standard deviation as noise signal ($T2_{\text{noise}}$, $T1_{\text{noise}}$, DWI_{noise}). For all ROI measurements, we always selected areas without obvious signs of bleedings (e.g. susceptibility artefacts in T2*-weighted images)



with 358 nm excitation and reading of blue fluorescence in the emitting 461 nm wave length spectrum representing the nuclear staining. Intensity as a surrogate for cell density was measured using the inherent intensity measurement function of Image J.

Statistical analysis

Comparisons between $Ki67_{\text{low}}$ and $Ki67_{\text{high}}$ tumours were performed using either Wilcoxon rank sum test and Pearson's chi-square test (for ordinal scaled or non-normal distributed values) or analysis of variance in case of normal distribution (tested by Shapiro–Wilk test). For multivariate

analyses, recursive partitioning conditional inference trees were built using R Software and the party package [22]. All other analyses were performed using JMP software solution (SAS, Cary, USA). For graphical illustrations, Affinity Designer (Serif (Europe) Ltd.) was used.

Results

Prediction of the primary cancer entity

Histological and clinical parameters (in particular CD31 + vessels, $Ki67\%$ and sex) had the potential to

differentiate BMs’ origins (Fig. 3). We found no evidence to support our hypothesis that clinically feasible MR morphological parameters may enable the stratification of the BM’s primary tumour entity. Multivariate analysis revealed that CD31-positive vessels with a cut-off set $> 101.5/\text{mm}^2$ could distinguish renal cell carcinomas from other entities ($p \leq 0.001$). Next, BM with CD31-positive vessels $\leq 101.5/\text{mm}^2$ showed a subdivision in the proliferation rate. BMs with a Ki67 $> 58.8\%$ were diagnosed either as SCLC, ‘others’, colorectal carcinomas or NSCLC ($p = 0.003$). BM of NSCLC mainly presented with a Ki67 $\leq 58.8\%$. Regardless, SCLC and ‘others’ mainly appeared in the Ki67 $> 58.8\%$ group. Malignant melanomas were only found with a Ki67 $\leq 58.8\%$ and equally distributed in gender. As expected, a differentiation of sex yielding breast cancer only appears in females ($p = 0.003$). Colorectal cancer was also found in the male cohort, with a Ki67 $\leq 58.8\%$. As mentioned above, NSCLC was mostly seen in Ki67 $\leq 58.8\%$ patients, but with a predominance in males.

Proliferation rate defines two distinct subsets of BM

After failing to predict BM’s primary tumour based on MR imaging features obtained from standard-of-care imaging, we further analysed patterns associated with the proliferative differences in BM’s.

Therefore, our next step was a dichotomisation (median-split) of our BM cohort in Ki67_{high} and Ki67_{low} subgroups. BMs with a Ki67 $> 27.9\%$ and $\leq 27.9\%$ were included in the Ki67_{high} and Ki67_{low} group, respectively. We observed that highly proliferative BM (Ki67_{high}) revealed a significantly bigger tumour size ($p = 0.0244$, Fig. 4, Table 1) and a smaller peritumoural oedema (Fig. 4, Table 1) than low-proliferative BM (Ki67_{low}). However, most ROI-based MR morphological parameters did not differ significantly between Ki67_{high} and Ki67_{low} BM (nT2_{mean}, T2_{CNR}, nT1_{mean}, T1_{CNR}, nDWI_{mean}, Table 1). In fact, only DWI_{CNR} was significantly higher in the Ki67_{high} BM group which should represent a stronger intratumoural diffusion restriction than in Ki67_{low} BM ($p = 0.0321$, Fig. 4, Table 1). Accordingly, Ki67_{high} BM revealed lower nADC_{mean} values ($p = 0.0035$, Fig. 4, Table 1).

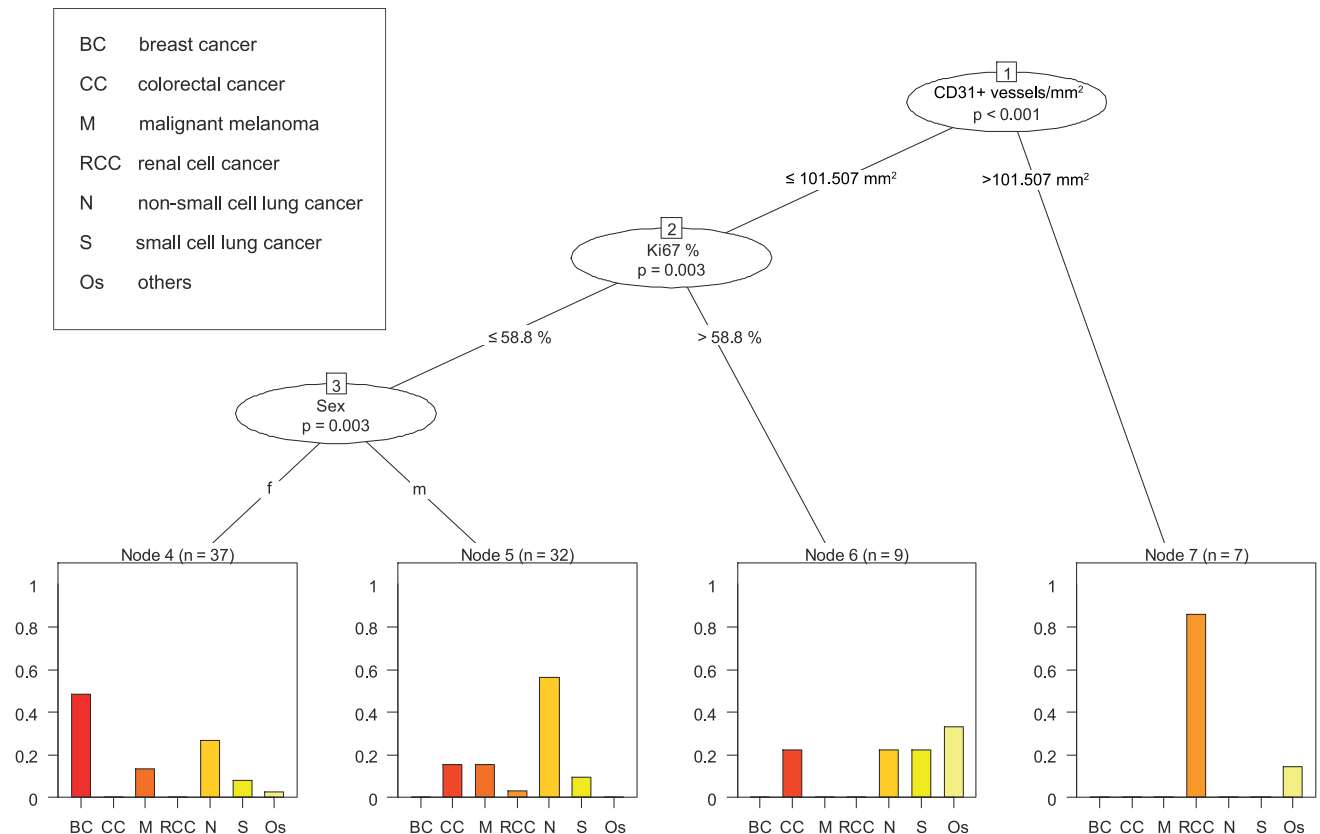


Fig. 3 Decision tree to stratify the brain metastases’ primary tumour entity. Multivariate analysis using recursive partitioning conditional inference trees with histopathological and MRI variables as predictors of brain metastases’ primary tumour entity

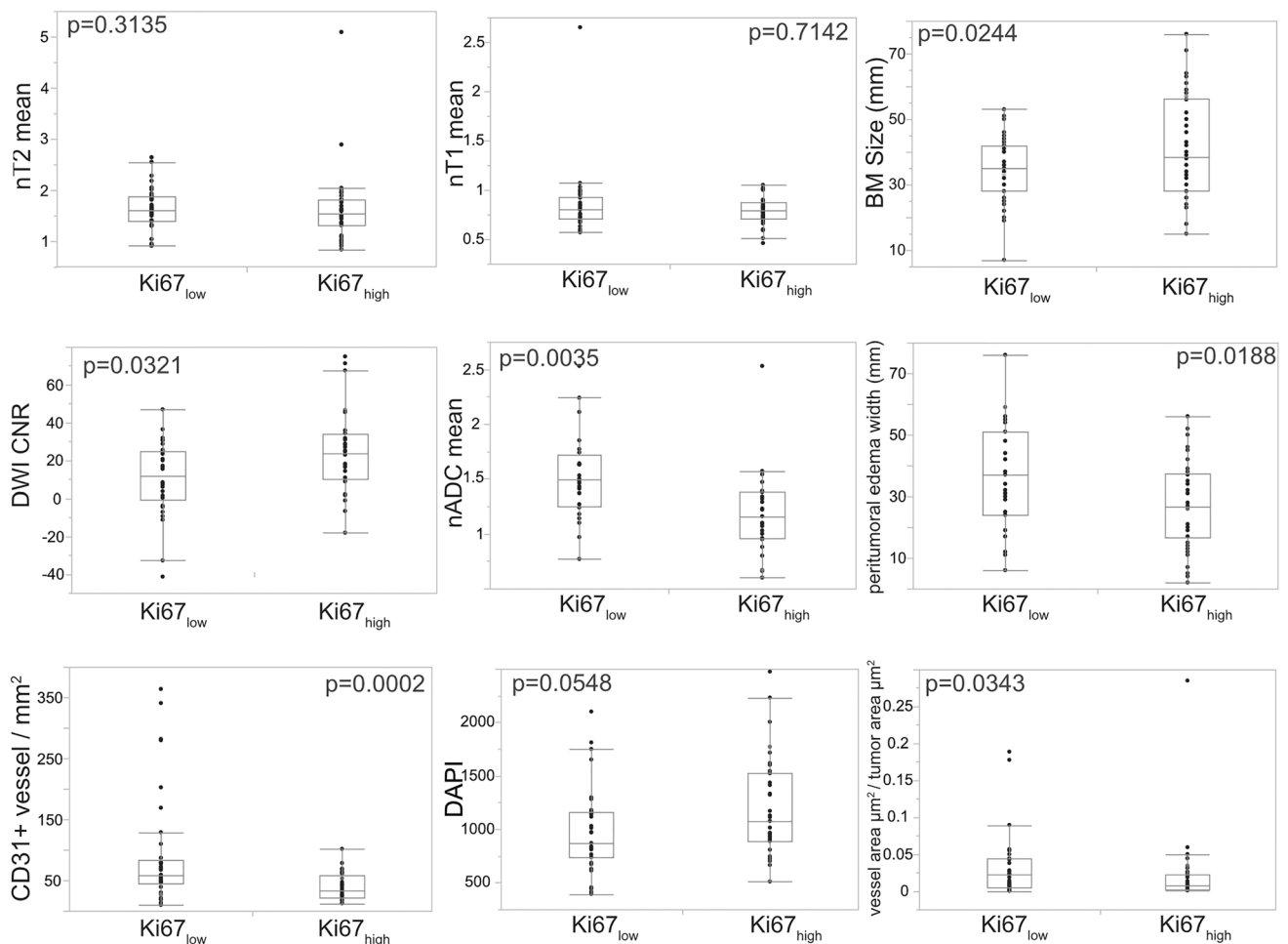


Fig. 4 Imaging and histopathologic features differ according to the brain metastasis' proliferation rate. Magnet resonance imaging and histopathological features in brain metastases stratified by proliferative capacity (Ki67_{high} and Ki67_{low} subgroups)

By histopathological assessment, we found that both microvessel density (CD31-positive vessels/mm²) and vessel area (vessel area/tumour area) were reduced in the Ki67_{high} BM cohort ($p=0.0002$; $p=0.0343$, Fig. 4, Table 1). Cell density assessed by DAPI nuclear staining showed a strong trend towards a higher cell density in Ki67_{high} BM ($p=0.0548$, Fig. 4, Table 1).

BM of SCLC and NSCLC as examples for Ki67_{high} and Ki67_{low} BM

As BM of NSCLC and SCLC mainly differed in their proliferative capacity and the distinction of these two lung cancer types is of major clinical relevance, we further analysed their MRI and histological parameters. BMs of SCLC ($n=8$) were represented by the Ki67_{high} BM features, while NSCLC BM ($n=30$) showed the pattern of the Ki67_{low} group ($p=0.0119$, Fig. 5a). BMs of SCLC were larger ($p=0.0008$, Fig. 5a) and showed a smaller peritumoural oedema width ($p=0.0148$,

Fig. 5a) than BM of NSCLC. Additionally, BM of SCLC showed stronger signs of diffusion restrictions by higher DWI_{CNR} signals ($p=0.0329$, Fig. 5a) and lower nADC_{mean} values ($p=0.0017$, Fig. 5a). On histological level, cell density (assessed by DAPI staining) was increased in BM of SCLC compared to BM of NSCLC ($p=0.0057$, Fig. 5a).

Discussion

In our study, we aimed to decipher MR morphological patterns of BM, to presurgically differentiate the BM's primary tumours and to obtain biological validation by matched histological analyses.

While BMs' MR morphology did not allow a prediction of their origin, we found different MRI features for high-proliferative (Ki67_{high}) and low-proliferative (Ki67_{low}) BMs that might help to distinguish BM deriving from NSCLC

Table 1 Comparison of clinical data, magnetic resonance imaging and histological parameters of the dichotomised Ki67_{high} and Ki67_{low} brain metastases cohort

Variable		Ki67 ^{high} median (range) or <i>n</i> (%) or mean ± SD (CI)	Ki67 ^{low} median (range) or <i>n</i> (%) or mean ± SD (CI)	<i>p</i> -value
Patient age in years (range)		60 (33–81)	62 (13–80)	0.4206 [#]
BM number (range)		1 (1–7)	1 (1–14)	0.9412 [#]
Sex	Male	16 (21.51%)	21 (24.73%)	0.3026 ^{##}
	Female	22 (27.96%)	18 (25.81%)	
Localization	Supratentorial	21 (27.27%)	27 (35.06%)	0.2060 ^{##}
	Infratentorial	17 (22.08%)	12 (15.58%)	
KPS (%)		80 (20–100)	80 (30–100)	0.7471 ^{###}
BM size in mm (range)		41.39 ± 15.35 (37.19–45.59)	34.58 ± 10.18 (31.29–37.89)	*0.0244 ^{###}
Peritumoural oedema according to Spanberger et al. [9]	Grade 1	3 (3.90%)	1 (1.30%)	*0.0435 ^{##}
	Grade 2	15 (19.48%)	7 (9.09%)	
	Grade 3	20 (25.97%)	31 (40.26%)	
Peritumoural oedema according to Tung et al. [19]	Ratio	76.37 (3.45–335.48)	112.12 (26.97–283.87)	0.0367 [#]
	Width in mm (range)	26.5 (2–56)	37 (7–76)	0.0188 [#]
<i>nT2</i> _{mean} (range)		1.55 (0.84–5.09)	1.61 (0.91–2.64)	0.3135 [#]
<i>T2</i> _{CNR} (range)		26.23 (–7.76–150.54)	24.70 (–17.77–172.31)	0.9008 [#]
<i>nT1</i> _{mean} (range)		0.79 (0.46–1.05)	0.8 (0.57–2.65)	0.7142 [#]
<i>T1</i> _{CNR} (range)		–20.3 (–69.89–8.08)	–13.48 (–77.69–46.79)	0.2747 [#]
<i>nDWI</i> mean (range)		1.43 (0.58–2.87)	1.315 (0.63–3.22)	0.3632 [#]
<i>DWI</i> _{CNR} (range)		23.755 (–18.17–74.93)	11.925 (–41.39–46.93)	0.0321 [#]
<i>nADC</i> _{mean} (range)		1.13 (0.6–2.53)	1.48 (0.77–2.53)	0.0035 [#]
$\frac{\text{vesselarea } \mu\text{ m}^2}{\text{tumourarea } \mu\text{ m}^2}$ (range)		0.0079 (0.0004–0.2849)	0.0224 (0.00004–0.1886)	0.0343 [#]
$\frac{\text{CD31+vessels}}{\text{mm}^2}$ (range)		33.19 (12.34–101.51)	59.16 (9.73–363.67)	0.0002 [#]
DAPI		1075.56 (510.06–2473.66)	868.47 (345.78–2099.89)	0.0548 [#]

DAPI (4',6-diamidino-2-phenylindole). DWI (diffusion-weighted imaging). ADC (apparent diffusion coefficient). CD (cluster of differentiation). CNR (contrast-to-noise ratio). SD (standard deviation). CI (confidence interval). Age is indicated in years. KPS (Karnofsky Performance Status) is indicated in percentage (%). Brain metastasis (BM) size and peritumoural oedema width are indicated in mm. All values are labelled as median (range) or *n* (%) or mean ± standard deviation (CI). Significant *p*-values with *p* < 0.05 are indicated by *. [#]Wilcoxon rank sum test; ^{##}Pearson's chi-square; ^{###}analysis of variance was performed due to normal distribution, tested with Shapiro–Wilk test

(Ki67_{low}) and SCLC (Ki67_{high}), an issue of special clinical interest facing the different treatment strategies. Therefore, the identified MR characteristics may serve as a non-invasive diagnostic tool to guide diagnostic and therapeutic decision making in patients with inoperable lung cancer and inconclusive biopsy of the primary tumour. SCLC BMs as representatives of the Ki67_{high} group were characterised by smaller surrounding oedema, despite a larger tumour size, in contrast to BMs from NSCLC reflecting the features of the Ki67_{low} group. These results seem counterintuitive at first, since an increasing peritumoural oedema has long been recognised as an important cause of morbidity and mortality in patients with metastatic lesions [9]. However, there are other examples of fast and aggressive growing brain

tumours with little amounts of peritumoural oedema, for example, the group of tumours formerly known as primitive neuroectodermal tumours, atypical teratoid/rhabdoid tumours and primary central nervous system lymphomas. These highly proliferative tumours are characterised by a relatively small peritumoural oedema compared to their large tumour size [23–29]. It may be assumed that processes of vascular remodelling or less time for angiogenesis might be reasons for the limited peritumoural oedema extent of faster growing BM. It has been evaluated that along with the brain invasion of the metastatic cells, angiogenic factors, such as vascular endothelial growth factor [30], might be released inducing the formation of new, but more leaky vessels [31]. However, as it has recently been shown for melanoma, BMs perform

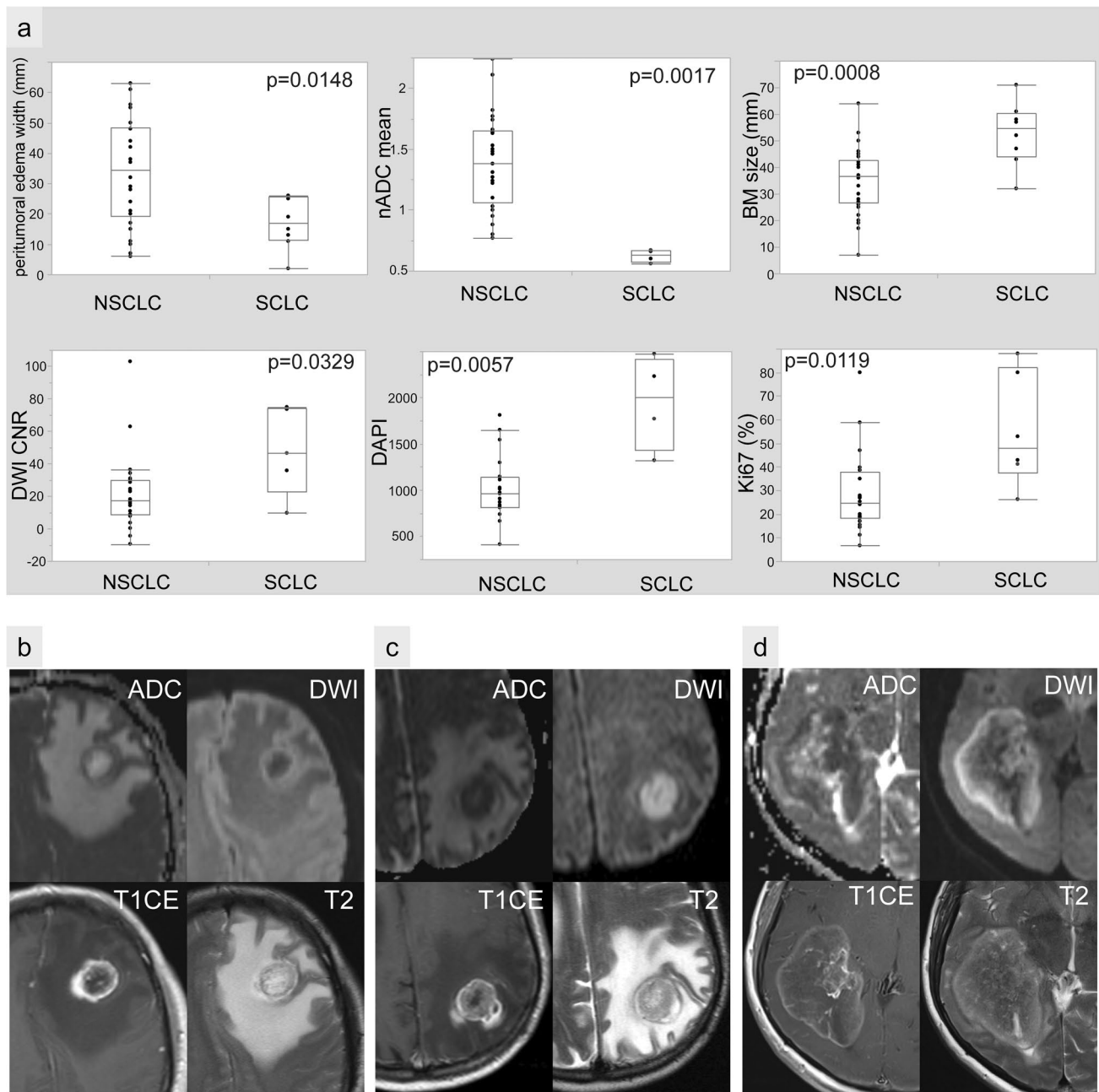


Fig. 5 Imaging and histopathologic features differ in NSCLC versus SCLC brain metastasis. **a** Comparison of magnetic resonance imaging features and histopathological parameters in non-small-cell lung cancer (NSCLC) and small-cell lung cancer (SCLC) brain metastases. According to our findings, SCLC (**d**) usually show stronger signs

of diffusion restrictions with reduced values in the ADC map, a bigger tumour size as well as a small peritumoural oedema rim compared to brain metastasis of NSCLC (**b**). Nevertheless, there are brain metastases that do not reflect these typical morphological findings, exemplified on a NSCLC brain metastasis (**c**)

vascular remodelling by co-opting existing blood vessels [32, 33]. Similar to our results, Spanberger et al. [9] also found a lower mean vessel density and a lower angiogenic potential in BM with small peritumoural oedema together with a shortened patient survival. The group of Ki67_{high} BM also showed diffusion restriction with respective lower ADC values. Diffusion restriction, which means restricted diffusion

of water protons in extracellular spaces, is quantified by ADC values [11]. Further, we showed that the increased diffusion restriction was associated with a trend towards an increased cellular density in Ki67_{high} BM. It has been shown before that a higher cellularity of tumours, defined as the number of cells in a given area of tumour tissue, narrows the extracellular space and limits the water diffusion [12, 13]. The extracellular

water inside the tumour may also be reduced by the lower amount of permeable vasculature in Ki67_{high} BM.

In line with our findings, Berghoff et al. [10] found a correlation between the diffusion restriction and a high proliferation index (Ki67%). Furthermore, they observed a higher amount of interstitial reticulin fibres in BM presenting with signs of higher diffusion restrictions. We found no difference regarding reticulin fibres among Ki67_{high} and Ki67_{low} tumours (data not shown). Our study has limitations that warrant discussion. Due to the retrospective nature of our investigation, we faced MRIs with differing protocols, field strengths, contrast media protocols/timing and a rather small cohort size. Thus, generalisability might be limited. The sample size differed in NSCLC ($n=30$) versus SCLC ($n=8$) patients which might have affected the results. Larger prospective studies are warranted to disclose the relationships between the metastatic growth/proliferation and the associated structural alterations of the brain microenvironment including the neurovascular network. All ROIs were related to an internal reference and CNR was assessed whenever possible in order to allow comparability in a most standardised and objective fashion. We did not perform computerised tumour volume segmentation for the calculation of the BM size [34] and we did not calculate high-dimensional radiomics as we faced highly heterogeneous real-world data and aimed to develop a clinically feasible step-by-step approach. We chose this approach since we aimed to use interpretable MR imaging features assessable in everyday clinical practice. Last, we focused on MRI measurements; therefore, the analysis of the spatial distribution of brain metastases was beyond the scope of our manuscript [35, 36].

In conclusion, we were not able to stratify a specific MRI pattern predicting BM origin. However, we detected distinct MRI features and histopathological profiles with regard to low- (Ki67_{low}) and high-proliferative (Ki67_{high}) BM. These features might have the potential to non-invasively differentiate NSCLC and SCLC BM in a daily routine workflow.

Acknowledgements MM would like to thank the Luxembourg National Research Fond (FNR: PEARL P16/BM/11192868 grant). PSZ has received intramural funding by the FFF program ‘Nachwuchswissenschaftler’ and ‘Patenschaftsprogramm’ as well as within the ‘Clinician Scientist Program’ by the Mildred-Scheel Foundation. The Dr. Senckenberg Institute of Neurooncology is supported by the Dr. Senckenberg Foundation. JPS has received funding by the State of Hessen within the LOEWE program.

Author contribution All authors contributed to the study conception and design. Material preparation, data collection and analysis were performed by MK, EH, JR, PSZ, JPS, M-TF, KHP, TJV, EH, MM, SB, PNH and SB. The first draft of the manuscript was written by MK, SB, PNH and SB, and all authors commented on previous versions of the manuscript. All authors read and approved the final manuscript and agree to be accountable for all aspects of the work in ensuring that questions related to the accuracy or integrity of any part of the work are appropriately investigated and resolved.

Funding Open Access funding enabled and organized by Projekt DEAL.

Data Availability Data is available upon reasonable request from the corresponding author.

Declarations

Competing interests The authors have no financial support or relationships that may pose a conflict of interest.

Ethics approval Tissue/tumour samples and/or patient data used in this study were provided by the University Cancer Center Frankfurt (UCT). Written informed consent was obtained from all patients and the study was approved by the Institutional Review Boards of the UCT and the Ethical Committee at the University Hospital Frankfurt (GS 4/09; project-number: SNO-04–2015).

Consent to participate Informed consent was obtained from all individual participants included in the study.

Consent to publish Patients signed informed consent regarding publishing their data and photographs.

Open Access This article is licensed under a Creative Commons Attribution 4.0 International License, which permits use, sharing, adaptation, distribution and reproduction in any medium or format, as long as you give appropriate credit to the original author(s) and the source, provide a link to the Creative Commons licence, and indicate if changes were made. The images or other third party material in this article are included in the article’s Creative Commons licence, unless indicated otherwise in a credit line to the material. If material is not included in the article’s Creative Commons licence and your intended use is not permitted by statutory regulation or exceeds the permitted use, you will need to obtain permission directly from the copyright holder. To view a copy of this licence, visit <http://creativecommons.org/licenses/by/4.0/>.


References

1. Preusser M, Capper D, Ilhan-Mutlu A, Berghoff AS, Birner P, Bartsch R et al (2012) Brain metastases: pathobiology and emerging targeted therapies. *Acta Neuropathol (Berl)* 123:205–22. <https://doi.org/10.1007/s00401-011-0933-9>
2. Davis FG, Dolecek TA, McCarthy BJ, Villano JL (2012) (2012) Toward determining the lifetime occurrence of metastatic brain tumors estimated from 2007 United States cancer incidence data. *Neuro-Oncol* 14:1171–1177. <https://doi.org/10.1093/neuonc/nos152>
3. Taillibert S, Le Rhun É (2015) Epidemiology of brain metastases. *Cancer Radiother J Soc Francaise Radiother Oncol* 19:3–9. <https://doi.org/10.1016/j.canrad.2014.11.001>
4. Sperduto PW, Kased N, Roberge D, Xu Z, Shanley R, Luo X et al (2012) Summary report on the graded prognostic assessment: an accurate and facile diagnosis-specific tool to estimate survival for patients with brain metastases. *J Clin Oncol Off J Am Soc Clin Oncol* 30:419–425. <https://doi.org/10.1200/JCO.2011.38.0527>
5. Faehndrich J, Weidauer S, Pilatus U, Oszvald A, Zanella FE, Hattungen E (2011) Neuroradiological viewpoint on the diagnostics of space-occupying brain lesions. *Clin Neuroradiol* 21:123–139. <https://doi.org/10.1007/s00062-011-0073-6>

6. Lee EK, Lee EJ, Kim MS, Park H-J, Park NH, Park SI et al (2012) Intracranial metastases: spectrum of Mr imaging findings. *Acta Radiol* 53:1173–1185. <https://doi.org/10.1258/ar.2012.120291>
7. Hirano H, Yokoyama S, Yunoue S, Yonezawa H, Yatsushiro K, Yoshioka T et al (2014) MRI T2 hypointensity of metastatic brain tumors from gastric and colonic cancers. *Int J Clin Oncol* 19:643–648. <https://doi.org/10.1007/s10147-013-0596-8>
8. Oshiro S, Tsugu H, Komatsu F, Abe H, Ohmura T, Sakamoto S et al (2008) Metastatic adenocarcinoma in the brain: magnetic resonance imaging with pathological correlations to mucin content. *Anticancer Res* 28:407–413
9. Spanberger T, Berghoff AS, Dinhof C, Ilhan-Mutlu A, Magerle M, Hutterer M et al (2013) Extent of peritumoral brain edema correlates with prognosis, tumoral growth pattern, HIF1a expression and angiogenic activity in patients with single brain metastases. *Clin Exp Metastasis* 30:357–368. <https://doi.org/10.1007/s10585-012-9542-9>
10. Berghoff AS, Spanberger T, Ilhan-Mutlu A, Magerle M, Hutterer M, Woehrer A, et al (2013) Preoperative diffusion-weighted imaging of single brain metastases correlates with patient survival times. Zhan W, editor. *PLoS One*. 8:e55464
11. Backens M (2015) Grundlagen und Technik der diffusionsgewichteten MR-Bildgebung und der Diffusions-Tensor-Bildgebung. *Radiol* 55:762–770. <https://doi.org/10.1007/s00117-015-0004-7>
12. Sugahara T, Korogi Y, Kochi M, Ikushima I, Shigematu Y, Hirai T et al (1999) Usefulness of diffusion-weighted MRI with echoplanar technique in the evaluation of cellularity in gliomas. *J Magn Reson Imaging JMRI* 9:53–60
13. Guo AC, Cummings TJ, Dash RC, Provenzale JM (2002) Lymphomas and high-grade astrocytomas: comparison of water diffusibility and histologic characteristics. *Radiology* 224:177–183. <https://doi.org/10.1148/radiol.2241010637>
14. Surov A, Gottschling S, Mawrin C, Prell J, Spielmann RP, Wienke A et al (2015) Diffusion-weighted imaging in meningioma: prediction of tumor grade and association with histopathological parameters. *Transl Oncol* 8:517–523. <https://doi.org/10.1016/j.tranon.2015.11.012>
15. Arvinda HR, Kesavadas C, Sarma PS, Thomas B, Radhakrishnan VV, Gupta AK et al (2009) Glioma grading: sensitivity, specificity, positive and negative predictive values of diffusion and perfusion imaging. *J Neurooncol* 94:87–96. <https://doi.org/10.1007/s11060-009-9807-6>
16. Calvar JA, Meli FJ, Romero C, Calcagno ML, Yáñez P, Martínez AR et al (2005) Characterization of brain tumors by MRS, DWI and Ki-67 labeling index. *J Neurooncol* 72:273–280. <https://doi.org/10.1007/s11060-004-3342-2>
17. Goldberg SB, Contessa JN, Omay SB, Chiang V (2015) Lung cancer brain metastases. *Cancer J Sudbury Mass* 21:398–403. <https://doi.org/10.1097/PPO.0000000000000146>
18. Karnofsky D, Burchenal J (1949) The clinical evaluation of chemotherapeutic agents in cancer. 191–205
19. Tung GA, Rogg JM, Julius BD (2003) MRI of intracerebral hematoma: value of vasogenic edema ratio for predicting the cause. *Neuroradiology* 45:357–362. <https://doi.org/10.1007/s00234-003-0994-0>
20. Hayashida Y, Hirai T, Morishita S, Kitajima M, Murakami R, Korogi Y et al (2006) Diffusion-weighted imaging of metastatic brain tumors: comparison with histologic type and tumor cellularity. *Am J Neuroradiol* 27:1419–1425
21. Harter PN, Zinke J, Scholz A, Tichy J, Zachskorn C, Kvasnicka HM et al (2014) (2014) Netrin-1 expression is an independent prognostic factor for poor patient survival in brain metastases. *PLoS One* 9:e92311. <https://doi.org/10.1371/journal.pone.0092311>
22. Hothorn T, Hornik K, Zeileis A (2006) Unbiased recursive partitioning: a conditional inference framework. *J Comput Graph Stat* 15:651–674. <https://doi.org/10.1198/106186006X133933>
23. Schwaighofer BW, Hesselink JR, Press GA, Wolf RL, Healy ME, Berthoty DP (1989) Primary intracranial CNS lymphoma: MR manifestations. *AJNR Am J Neuroradiol* 10:725–729
24. Davis PC, Wichman RD, Takei Y, Hoffman JC (1990) Primary cerebral neuroblastoma: CT and MR findings in 12 cases. *AJNR Am J Neuroradiol* 11:115–120
25. Koeller KK, Smirniotopoulos JG, Jones RV (1997) Primary central nervous system lymphoma: radiologic-pathologic correlation. *Radiogr Rev Publ Radiol Soc N Am Inc* 17:1497–1526
26. Chawla A, Emmanuel JV, Seow WT, Lou J, Teo HE, Lim CCT (2007) Paediatric PNET: pre-surgical MRI features. *Clin Radiol* 62:43–52. <https://doi.org/10.1016/j.crad.2006.09.008>
27. Lee IH, Yoo S-Y, Kim JH, Eo H, Kim OH, Kim I-O et al (2009) Atypical teratoid/rhabdoid tumors of the central nervous system: imaging and clinical findings in 16 children. *Clin Radiol* 64:256–264. <https://doi.org/10.1016/j.crad.2008.09.007>
28. Fruehwald-Pallamar J, Puchner SB, Rossi A, Garre ML, Cama A, Koelblinger C et al (2011) Magnetic resonance imaging spectrum of medulloblastoma. *Neuroradiology* 53:387–396. <https://doi.org/10.1007/s00234-010-0829-8>
29. Zhang S, Li H, Zhu R, Zhang M (2016) Application value of magnetic resonance imaging in diagnosing central nervous system lymphoma. *Pak J Med Sci* 32:389–393
30. Yano S, Shinohara H, Herbst RS, Kuniyasu H, Bucana CD, Ellis LM et al (2000) Expression of vascular endothelial growth factor is necessary but not sufficient for production and growth of brain metastasis. *Cancer Res* 60:4959–4967
31. Strugar J, Rothbart D, Harrington W, Criscuolo GR (1994) Vascular permeability factor in brain metastases: correlation with vasogenic brain edema and tumor angiogenesis. *J Neurosurg* 81:560–566. <https://doi.org/10.3171/jns.1994.81.4.0560>
32. Kienast Y, von Baumgarten L, Fuhrmann M, Klinkert WEF, Goldbrunner R, Herms J et al (2010) Real-time imaging reveals the single steps of brain metastasis formation. *Nat Med* 16:116–122. <https://doi.org/10.1038/nm.2072>
33. Fazakas C, Wilhelm I, Nagyoszi P, Farkas AE, Haskó J, Molnár J et al (2011) Transmigration of melanoma cells through the blood-brain barrier: role of endothelial tight junctions and melanoma-released serine proteases. *PLoS One* 6:e20758. <https://doi.org/10.1371/journal.pone.0020758>
34. Lacroix M, Abi-Said D, Fournay DR, Gokaslan ZL, Shi W, DeMonte F et al (2001) A multivariate analysis of 416 patients with glioblastoma multiforme: prognosis, extent of resection, and survival. *J Neurosurg* 95:190–198
35. Quattrocchi CC, Errante Y, Gaudino C, Mallio CA, Giona A, Santini D et al (2012) Spatial brain distribution of intra-axial metastatic lesions in breast and lung cancer patients. *J Neurooncol* 110(1):79–87. <https://doi.org/10.1007/s11060-012-0937-x>
36. Takano K, Kinoshita M, Takagaki M, Sakai M, Tateishi S, Achiha T et al (2016) Different spatial distributions of brain metastases from lung cancer by histological subtype and mutation status of epidermal growth factor receptor. *Neuro Oncol* 18(5):716–724. <https://doi.org/10.1093/neuonc/nov266>

Publisher's note Springer Nature remains neutral with regard to jurisdictional claims in published maps and institutional affiliations.

Authors and Affiliations

Makoto Kiyose^{1,2,3,4} · **Eva Herrmann**⁵ · **Jenny Roesler**⁶ · **Pia S. Zeiner**^{2,3,4,7,8,9} · **Joachim P. Steinbach**^{3,4,7,8,9} · **Marie-Therese Forster**¹⁰ · **Karl H. Plate**^{6,8,9} · **Marcus Czabanka**¹⁰ · **Thomas J. Vogl**¹¹ · **Elke Hattingen**¹ · **Michel Mittelbronn**^{6,12,13,14,15,16,17} · **Stella Breuer**¹ · **Patrick N. Harter**^{6,8,9} · **Simon Bernatz**^{3,4,6,11} 

¹ Institute of Neuroradiology, University Hospital, Goethe University, Frankfurt am Main, Germany

² Department of Neurology, University Hospital, Frankfurt am Main, Germany

³ Frankfurt Cancer Institute (FCI), Goethe University, Frankfurt am Main, Germany

⁴ University Cancer Center Frankfurt (UCT), University Hospital, Goethe University, 60590 Frankfurt am Main, Germany

⁵ Institute for Biostatistics and Mathematical Modelling, University Hospital, Frankfurt am Main, Germany

⁶ Neurological Institute (Edinger Institute), University Hospital, Frankfurt, Frankfurt am Main, Germany

⁷ Senckenberg Institute of Neurooncology, University Hospital, Frankfurt am Main, Germany

⁸ German Cancer Consortium (DKTK), Heidelberg, Germany

⁹ German Cancer Research Centre (DKFZ), Heidelberg, Germany

¹⁰ Department of Neurosurgery, Goethe University, Frankfurt am Main, Germany

¹¹ Department of Diagnostic and Interventional Radiology, University Hospital Frankfurt, Goethe University Frankfurt Am Main, Theodor-Stern-Kai 7, 60590 Frankfurt am Main, Germany

¹² Luxembourg Centre for Systems Biomedicine (LCSB), University of Luxembourg, Esch-sur-Alzette, Luxembourg

¹³ Laboratoire National de Santé (LNS), Dudelange, Luxembourg

¹⁴ Luxembourg Center of Neuropathology (LCNP), Dudelange, Luxembourg

¹⁵ Department of Cancer Research (DoCR), Luxembourg Institute of Health (L.I.H.), Luxembourg, Luxembourg

¹⁶ Department of Life Sciences and Medicine (DLSM), University of Luxembourg, Esch-sur-Alzette, Luxembourg

¹⁷ Faculty of Science, Technology and Medicine (FSTM)S, University of Luxembourg, Esch-sur-Alzette, Luxembourg